MAGNETIC CONTROL OF NANOEL VIA MAGNETO-MECHANICAL ACTUATION: A PROOF OF CONCEPT FOR A POTENTIAL NANOTHERAPEUTIC APPROACH

By

Mohammad Kanber

May 2023

Director of Thesis Dissertation: Juan Beltran-Huarac, PhD

DEPARTMENT OF PHYSICS

ABSTRACT

Cancer treatment is one of the major health problems that burdens society. According to the latest publication of the American Cancer Society, the cancer mortality rate has reached 32% in 2022 in the US. To address these alarming numbers, some gold standards, including therapeutic targeting, are being used to treat cancer. However, when tumor grows beyond a critical size, its vascular system differentiates abnormally and erratically creating heterogeneous endothelial barriers that further restricts drug deliveries into tumors. One way to overcome this problem is to induce endothelial leakiness using nanoparticles (NanoEL), so therapeutic drugs can be successfully delivered. While several methods exist, none has been established as a valid clinical approach. The most concerning complication is related to the fact that uncontrolled NanoEL prompts subsequent tumor migration and the appearance of new metastatic sites. In this research, we propose a new non-invasive approach based on magneto-mechanical actuation to remotely control the NanoEL by implementing PEGylated superparamagnetic iron oxide nanoparticles (PEG SPIONs), which are actuated by non-heating super low-frequency magnetic fields. As proof of concept, we developed a 2D cell culture model based on human umbilical vein endothelial cells (HUVEC).

Our findings indicate that PEG-SPIONs can assemble within the actin filaments. When magnetically actuated, magnetic forces are translated into mechanical agitation, which induced actin remodeling and subsequent disruption of VE-cadherin junctions. This enabled us to deliver therapeutic drugs across the endothelium in a controlled manner. This approach has the potential to avert cancer migration and provides a remotely controlled drug delivery method harnessing the physics and biology of endothelial adherens junctions. This approach can open up new avenues for targeted drug delivery into anatomic regions within the body for a broad range of disease interventions.

MAGNETIC CONTROL OF NANOEL VIA MAGNETO-MECHANICAL ACTUATION: A PROOF OF CONCEPT FOR A POTENTIAL NANOTHERAPEUTIC APPROACH

By

Mohammad Kanber

May 2023

A Thesis

Presented to the Faculty of the Department of Physics at

East Carolina University

In Partial Fulfillment of the Requirements for the Degree of

Masters of Science in Physics

Thesis Committee

Director of Thesis: Juan Beltran-Huarac, PhD

Thesis Committee Members:

Jefferson Shinpaugh, PhD

Nathan Hudson, PhD

Jitka Virag, PhD

ACKNOWLEDGEMENTS

I thank Dr. Juan Beltran-Huarac and all the lab members, especially Mr. Obum Umerah, Mr. John Cooper, and Mr. Robby Moller, for their guidance and resources they provided in every step of this project. I would also like to acknowledge Dr. Lewis Reynolds (North Carolina State University) for collecting the VSM data, Dr. Jared Brown and Mr. Stephen Brindley (University of Colorado) for collecting the ICP-MS data, Dr. Amar S. Kumbhar (UNC-Chapel Hill) for collecting the TEM images, and Ms. Maycie McDoughal for assisting with the FTIR measurements. Thanks, BioRender.com, for the free trial version of the software, which was used for some illustrations for this project.

TABLE OF CONTENTS

.

LIST OF TABLES

LIST OF FIGURES

LIST OF ABBREVIATIONS/SYMBOLS

CHAPTER 1: Tumor Targeting Using Nanotechnology

1.1 Current State of Tumor Targeting

Cancer is the leading cause of death worldwide according to the World Health Organization. Surgical removal is most effective when tumors are still in their early stages where it has not yet metastasized but limited into a confined space [1]. When surgical approach fails to control tumor growth, then chemotherapy and radiotherapy are considered [1]. While chemotherapy can be effective in killing cancer cells, its development suffers deadly and uncontrolled side effects because of its non-specific toxicity [2]. Nanomedicine , however, with the current development in nanotechnology can provide an alternative and a promising approach to minimize toxicity concerns [2]. Intravenous nanomedicine can be therapeutically effective when the therapeutic drugs it uses pass through the blood vessel barrier and reach their target sites, the cancerous cells. Otherwise, this method can induce detrimental side effects due to its poor efficacy [3]. The blood vessel wall characterized by the endothelium lining marks the main barrier for pharmacological drug treatment between the circulatory system and tissue spaces. This barrier is semipermeable and regulates tissue fluid homeostasis, allowing only selective extravasation of small molecules, solutes, and plasma proteins [4][5][6]. Therefore, the endothelial barriers formed within the tumor microenvironment may primarily account for the efficacy and the delivery uniformity of many FDA approved nanotherapeutics [7]. This chapter discusses the different methods that have been investigated to overcome the endothelial barrier and sheds light on why these methods have fallen short of advancing to clinical trials.

1.1.1 The EPR Effect: Advantages, Limitations, and Challenges. In an event of tumor proliferation, the endothelial barrier undergoes highly coordinated disconnection and remodeling of cell junctions, inducing intercellular gaps within the tumor vasculature, which gives rise to the enhanced permeability and retention (EPR) effect [1][3][4]. This effect is a unique phenomenon of solid tumors related to their anatomical and pathophysiological differences from normal tissues [1]. The EPR, which is not observed in normal conditions, can selectively allow macromolecules with sizes larger than 40 kDa to pass through the blood vessels and accumulate in the tumor mass [1]. For this reason, the EPR is considered the framework for enhancing tumor targeting in chemotherapy. The EPR effect was first proposed in 1986 by Matsumura and Maeda [8] and since then it had been extensively investigated as the main approach to deliver anti-cancer drugs across the endothelium [1][3]. In fact, the period from 1980 to 1990 is marked by early breakthroughs in drug delivery, specially delivering drugs into the tumor microenvironment through passive targeting [9]. SMANCS, a polymer conjugated to the anticancer protein neocarzinostatin, was the first drug that exploited the EPR effect via passive targeting. Konno et al observed that SMANCS is selectively accumulated in all clinically tested solid tumors [10]. While this approach exploits remarkably the leakiness of the tumor vascular system, it faces challenges associated with tumor microenvironment dependence, which is not consistently observed in all tumor types. This creates some hurdles related to the treatment of the whole tumor or even small metastatic sites. To illustrate this, consider the normal cell vasculature, which is sufficient for small tumors to maintain oxygen and nutrient supplies [11][12]. At early stages, the tumor will use the existing vasculature containing openings of <10 nm, through which the passage of macrodrugs is ineffective [4][11]. As the tumor grows to a size of 1-2 mm (the critical size), they shift from a balanced expression of stimulatory and inhibitory factors into a

more stimulatory growth expression [3][11][12]. This shift is known as the angiogenic switch. For sizes larger than the critical size, tumors must trigger the angiogenic switch to develop new vasculature [3][11][12]. This transition is characterized by the formation of abnormal architectures including twists, detours, deformities, and dead ends [3][11][12]. Abnormal vasculature can disrupt the blood flow within the tumor microenvironment, thereby creating hypoxic areas in the tumor mass [3][11][12]. Such hypoxic areas in turn increase the density of the abnormal vasculature system in a positive feedback loop, which is characterized by the upregulation of the vascular endothelial growth factor (VEGF) among others [3][11][12]. When the degree of EPR effect is related to the density of abnormal vasculature, the EPR effect can vary depending on tumor heterogeneity. This makes the EPR effect a complex model to be used in therapeutic targeting [3], therefore, new methods are needed to elicit endothelial permeability, so that therapeutic drugs can be successfully delivered into tumorous tissues.

1.2 NanoEL as an Approach for Tumor Targeting

Nanotechnology can play a pivotal role in finding innovative methods via the development of stimuli-responsive agents that can be remotely actuated to prompt cellular responses. More specifically, inorganic nanoparticles (NP) have shown a promising effect to cause nanomaterial-induced endothelial leakiness (NanoEL) through the disruption of adherens junctions [3][11]. These junctions mainly regulate and maintain the endothelial barrier [3]; they consist of vascular endothelial (VE)-cadherin and catenin proteins. The VE-cadherin extracellular domain of one cell can bind to another cis paired VE-cadherin in a homophilic trans interaction, whereas the intercellular domain counterpart shows a strong binding affinity to β-catenin [13]. As widely reported in the literature, VE-cadherin and actin filaments are dynamically linked either directly

via α-catenins or indirectly via linker proteins [13]. α-catenins can bind strongly to cadherin-β-catenin complex when it exists as a monomeric protein, whereas it preferably binds to actin when it exists as a dimer [4][14][15][16]. When α-catenin binds to actin filaments, it competes with the actin-related protein-2/3 complex (ARP2), which regulates the actin polymerization and filaments organization [4][14][15] [16]. This indicates that α-catenin is also involved in the regulation of VE-cadherin-catenin complex. In this regard, a more recent study has shown that when the mice VE-cadherin genes fused with the α-catenin showed strong resistance to vascular leakiness provided that certain induction factors (such as VEGF or histamine) are to be used [17]. Based on this, there is strong evidence on the link between acting filament remodeling and adherens junction regulation, which can be understood in terms of the NanoEL effect [4] [13][14][15][16]. The mechanistic aspect of this effect is governed by two chief approaches: (i) direct NP physical binding (type I) and (ii) indirect secondary effect (type II) including reactive oxygen species (ROS) production [3][11][18][19].

1.2.1 Type-I Induced NanoEL: Mechanism and Limitation. This mechanism is based on the ability negatively charged NPs has to disrupt the homophilic interaction of VE-cadherin by triggering the phosphorylation of Y658 and Y731 residues of VE-cadherin [18], which can lead to the disassembly of β-catenin and p120 catenin proteins. This can cause VE-cadherin to be digested by the cell and in turn induce actin filament remodeling [18]. This can be correlated to shape deformation, which increases the number of gaps between cells thereby resulting in leakiness. It is noteworthy that the interaction does not depend strongly on the nature of the NPs as much as it does on the physical connection between the VE-cadherin and NPs [18]. It was reported that NPs (unlike macroparticles) need to be small enough to migrate into the cell

junction to induce NanoEL effect [18]. More recently, some studies suggested that type-I NanoEL increases tumor migration and subsequent metastasis [11][20]. Peng and co-workers reported histology data indicating that new metastatic sites can appear in bone and liver when breast tumor-bearing mice are treated with NPs [20]. NPs significantly accelerated both intravasation and extravasation of breast cancer cells in animal models, increasing the extent of existing metastasis and its multiphasic processes. Such results accentuated the importance of NPs' behavior in complex biological systems, especially their stability in physiological media. Since leakiness depends on the probability a particle has to migrate into a junction niche and bind to VE-cadherin, random particle distribution will therefore result in random particle accumulation in one region over the other. This is consonant with the fact that the magnitude of leakiness depends on particle concentration [18][20].

1.2.2 Type-II Induced NanoEL: Mechanism and Limitation. This mechanism is mediated by the production of ROS, which is as an activator of the PI-3 kinase/Akt/GSK-3β signaling pathway that promotes microtubule remodeling and induces NanoEL [19]. However, ROS production poses cytotoxic effects, such as apoptotic pathway induction or DNA damage [11]. In addition, NPs can increase ROS expression followed by epithelial cell death, which is mediated by caspase activation after lipid peroxidation and lysosomal membrane destabilization events [21]. In this context, the existing methods in drug delivery, that use ROS-producing NPs, face some challenges and further investigation is needed.

CHAPTER 2: Magnetic Nanoparticles as Nanotherapeutics Alternatives

2.1 Iron Oxide Nanoparticles: Theory of Application and its Advantages

More recently, safe-by-design magnetic NPs have been proposed as alternatives to circumvent limitations in NanoEL. In particular, superparamagnetic iron oxide NPs (SPIONs) have received FDA approval and are being used as MRI contrast agents [22][23], MPI tracers [24], agents to treat iron deficiency [25], and actuators in cancer therapy [26]. When a weak exogeneous magnetic field is applied to SPIONs, it can shift all the particle magnetic moment to the direction of the field, which leads to a fast magnetic saturation. Turning the field off causes SPIONs to suppress their magnetic ordering, which can advert the risk of reciprocal attraction and agglomeration [27]. These observed characteristics are attributed to their superparamagnetic behavior. In principle, iron oxide commonly exits as magnetite (Fe_3O_4) or maghemite (γ-Fe_2O_3), in which both oxides exhibit ferromagnetic properties [28][29]. Ferromagnetic materials can become superparamagnetic by reducing the particles' physical size. A typical ferromagnetic material has multiple magnetic domains, each with a different associated magnetron. When these domains break up into single ones with diameter less than the diameter of a single domain (critical radius, r_c), the ferromagnetic materials are transformed into superparamagnetic ones [28][30]. This is due to the fact that the magnetic moments of a single domain can be uniformly magnetized and aligned with the external field (see Figure 1.1). Typically, this transformation occurs at certain radii (typically in the order of a few tens of nanometers) depending on the type of materials [28][30]. The transition area is referred to as the blocking temperature [29], where systemic magnetization can fluctuate because the thermal activation energy can overcome this

magnetic anisotropy barrier [31]. To this end, using SPIONs would be advantageous in terms of delivering controlled magnetic doses into a confined region in the 3D space.

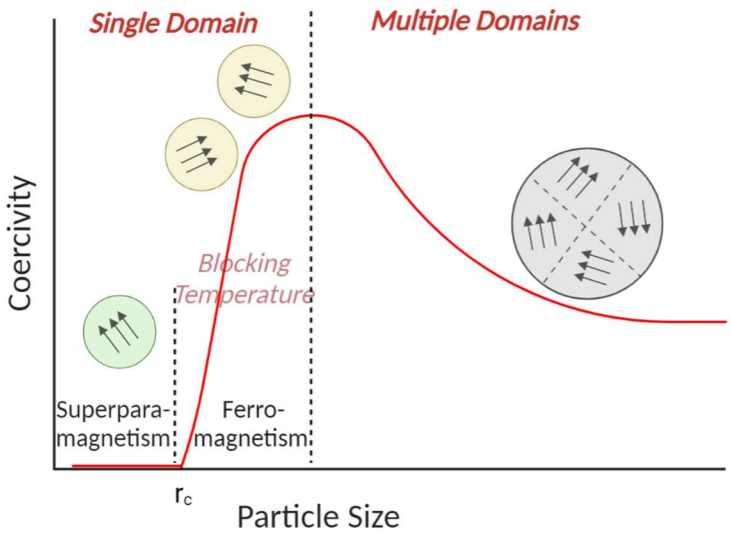

Figure 1.1 Coercivity of magnetic nanomaterials as a function of particle size. At the critical radius, ferromagnetic materials can exhibit superparamagnetic properties.

2.2 Iron Oxide Nanoparticles as Remote Actuators

The principle of magneto-mechanical actuation (MMA) is employed to induce a controlled stress force, and plays reportedly a pivotal role in manipulating cell signaling and function in magnetic hyperthermia and tissue engineering [26]. This requires cellular uptake of SPIONs. To make SPIONs stable in physiological environment, they are usually formulated with chains of poly-ethylene glycol (PEG), which also enables them to elude the immune system [26]. The size of nanoparticles is crucial to establish functional and powerful remote actuators because particle sizes are directly proportional to the magnitude of the induced magnetic torque and inversely proportional to the rate of cell uptake. A recent study indicated that the majority of research articles have reported less than 1% of particle delivery efficacy into solid tumors, which is

commonly ascribed to the physical properties of nanoparticles [32]. On the other hand, reducing the particle size to a certain critical size would prevent the effective physical motion of NPs when exposed to magnetic fields. To put this into perspective, consider a case when SPIONs are exposed to magnetic fields. Their magnetic moments shift into excited states. Typically, the system can lower its energy by either the Neel relaxation, where particles' magnetic moments start realigning intrinsically with the magnetic field (MF), causing no physical motion, or the Brownian relaxation, where the magnetic moments are extrinsically realigned as the particles rotate [33] [34].While both processes are complementary, Golovin et al proposed that the relaxation modes can be described as a function of particle core size. As this size increases, the Neel and Brownian relaxation times increase exponentially and linearly, respectively [33]. In the case of Fe_3O_4 NPs, the Brownian motion dominates, when the core size exceeds 7 nm [33]. Therefore, it is critical to choose a particle size that can be both internalized and strongly actuated. The maximum force (F_M) generated by a single magnetite nanoparticle can be described in terms of the strength of the magnetic field (B), particle saturation magnetization (J_S), density (ρ), hydrodynamic size (R_{HD}), and volume of the magnetic core (V_M), and is described by the following equation [34]:

$$F_M \approx 1.4\ \mu\ B/\ R_{HD} = 1.4\ J_s\ V_m\ \rho\ B/\ R_{HD} \quad (1)$$

The direct proportionality of F_M with the cubic power of the particle radius should explain the significance of choosing the right size. This system, however, only describes a single magnetite particle. Coated nanoparticles can aggregate into denser network as they translocate into the cell, especially when they are exposed to magnetic fields [34]. This can bring them into small proximity, thus enhancing their assembly. This can also increase the particle magnetic moment

(μ) by a factor of ($N \cdot \alpha$), which is related to the number of particles and the ordering of magnetic moments within the aggregate, respectively [34].

Another factor that can affect the MMA is the mode of magnetic exposure. A static magnetic field can induce a pulling force whereas oscillating magnetic field can generate a twisting force. It has been reported in the literature that the action-actin bond is more susceptible to break up by a twisting force rather than a pulling force. When 600 pN of straight pulling force is required, only 320 pN of twisting force is needed [34]. The theory of MMA has been implemented clinically in 2007 to treat local recurrence of prostate cancer. The technique is referred to as magnetic hyperthermia because magnetic torques encounter cell resistance, thus generating heat. It was also reported that increase in temperature (at and above 43°C) is enough to cause cancer cell damage [35]. This study showed tolerability with no systematic toxicity after 17.5 month follow-up [36]. Considering generated heat, any study of MMA should evaluate magnetic hyperthermia effects even though the frequencies used are in the order of kHz [34][35].

2.3 Magnetic Control of Endothelial Leakiness through Actuated Nanoparticles

As discussed in Chapter 1, NanoEL is an approach to enhance therapeutic targeting but is limited to either uncontrolled leakiness as in the Type-I approach or ROS production as in the Type-II approach. More recently, it was proposed that controlled NanoEL can be induced by magnetic forces. To illustrate this, PEG-SPIONs were used to show that the permeability of vascular endothelium can be increased using external static magnetic fields to transiently disrupt endothelial adherens junctions [6]. This can activate the paracellular transport pathway and facilitate local extravasation of circulating substances. While the full mechanism is still not clear,

a potential mechanism indicates preliminarily that PEG-SPIONs are linked to lysosomes, which in turn are associated with actin filaments [6]. which under magnetic field exposure suffer remodeling and subsequently VE-cadherin disruption. In addition, observations suggest that the endothelium can recover overnight in the form of adherens junction reconstruction and F-actin reorganization [6]. Even though the induction of magneto-mechanical stress can be mitigated overtime, this approach is limited to the use of static magnetic fields, which imposes a few clinical limitations. For instance, the magnetic force diminishes and drops rapidly with tissue depth [27][28]. This requires invasive surgeries to position a magnet in proximity with the target area. Another limitation is the fact that static fields are characterized by relatively uniform magnetic flux, whereas clinical electromagnet generators (*e.g.*, MRI scanners) use magnetic gradients, which can develop varying magnetic map in 3D space. Taken altogether, innovative methods that employ alternating magnetic fields to activate magnetic NPs, which can induce NanoEL, are needed to advance the field of drug delivery.

2.4 Theory of Application

Since the VE-cadherin junctions that hold the endothelial lining together are dynamically linked to the actin filaments, then inducing stress on these filaments can disrupt these junctions and lead to subsequent leakiness in the endothelium, which will allow therapeutic drug to pass through. In this work, we developed for the first time a new non-invasive method based on magneto-mechanical actuation to induce NanoEL using PEG-SPIONs. To prove this concept, we mimicked the endothelial cell barrier using a 2D cell culture model based on HUVEC cells. PEG-SPIONs can be actuated by non-heating magnetic fields. This can be achieved by using AC super low-frequency magnetic fields. The induced stress can be characterized in terms of the

particle hydrodynamic size (R_{HD}), particle core size (R_{np}), its saturation magnetization (J_S), and density (ρ) as described in equation 1. Therefore, physicochemical, morphological, and magnetic characterization of PEG-SPIONs is required. This will allow us to understand the MMA induced force in a biological setting.

CHAPTER 3: Methods and Procedures

3.1 Physicochemical Characterization Procedures.

3.1.1 Transmission Electron Microscopy. The principle of this microscopic technique is to accelerate electrons to high speeds and let them pass through a very thin sample. The beam of electrons transmitted through the sample can provide information about the morphology, size, structure, and distribution of nanoparticles in the sample. Therefore, the sample thickness needs to be tiny so the sample can be semitransparent to the beam, otherwise, it will be largely absorbed and detailed information of sample can be lost. This is easily achieved in liquid samples, which are directly placed onto copper TEM grids. In the case of solid samples, microtoming is used to slice up the sample into thin pieces.

For our specific measurements, samples consisting of aqueous solutions of PEG-SPIONs (1 μg/ml) were imaged using a Thermofisher Talos F200X Transmission Electron Microscopy (TEM) at an accelerating voltage of 200kV with Energy-Dispersive X-ray Spectroscopy (EDS) capabilities. Elemental composition of the samples was obtained from EDS in the form of spectroscopic distribution. For quantitative analysis of particle size, imageJ software was used; image scale bar was used as a calibration standard to find the relative size of imaged particles, then data were sorted out in a bar chart. Particle size distribution was obtained by fitting data to a normal distribution scaled to 100%.

3.1.2 Fourier Transform Infrared Spectroscopy. The principle of this spectroscopic technique lies in the use of infrared radiation that passes through a sample, which has vibrational energy levels characteristic of molecules. This radiation excites the molecules on the samples to higher energy states once is fully absorbed. Since each functional group absorbs selectively radiation at a specific wavelength, then the identity of the sample's chemical composition can be determined. For our specific measurement, 100 μl of aliquoted samples (1mg/ml solution) was placed on barium fluoride window of a Bruker LUMOSS II Fourier Transform Inferred (FTIR) microscope with focal plane array detector (FPA). This enabled us to obtain the modes of vibration of molecules (in our case, PEG) on the particle surfaces. Attenuated total reflection with video guided measurements were obtained using the OPUS software.

3.1.3 Vibrating Sample Magnetometry. This technique measures the variation of the magnetic flux using coils adjacent to sample holder that is subjected to vibration. The sample is also subjected to a constant magnetic field, however, when the sample has a dipole moment, it aligns with the external field, which will create a magnetic field, and this magnetic field can vary with time as the sample holder oscillates due to the change of the external magnetic force vector in space.

For our specific measurements, the magnetic moment of PEG-SPIONs powders were evaluated as a function of the magnetic field strength at 300K using the vibrating sample magnetometer (VSM) with resolution of ~$3x10^{-8}$ emu. The magnetic fields were applied in the range $\mp$ 5 T. The samples (~1mg) were placed in polypropylene VSM sample holders (part num. 4096-388, Quantum Design, Inc.) before collecting data.

3.1.4 Dynamic Light Scattering and Zeta Potential. This technique uses the idea that individual particles have unique randomness as they move in the solvent under Brownian motion. When light hits individual particles, the resultant scattered light will also have phase randomness. When the fluctuation of the scattered light is measured in a time dependent manner, then its intensity fluctuation can be correlated to the hydrodynamic size. Smaller particles move faster; hence, more fluctuation will be observed when compared to larger particles.

As for zeta potential, a voltage is applied to the sample, which can ionize the particles and in turn they can attract opposite ions. This will make an ionic shell around the individual particle that is referred to as the Stern layer. As we go further away from the particle, the opposite charge ions will get more loosely attached until we reach what is called the slipping plane, where solvent ions are no longer attached to the particle-solvent shell. The zeta potential is defined at the voltage of the slipping plane in relationship to a bulk point in the solvent away from the particle.

For hydrodynamic size measurement, 100 ug/ml of PEG-SPIONs in EBM-2 was aliquoted in DTS0012 cuvettes. For zeta potential measurements, 100 ug/ml of PEG-SPIONs in ultra-high pure water was aliquoted in DTS1070 cuvettes. Particle refractive index was assumed to be 2.36 and its absorption was set to 0.147. Measurements were obtained at 25°C using the Zetasizer Pro Red from Malvern Panalytical, and data were analyzed by ZS xplorer software.

3.2 Biological Assays

Human umbilical vein endothelial cells (HUVECs) were cultured in EBM-2 cell medium with EGM-2 supplements until 95-100% confluent. Then cells were treated and incubated with PEG-SPIONs solution of appropriate concentration for 3 hours at 37° C to allow internalization.

3.2.1 Cell Uptake. Cell uptake studies investigated the internalization of PEG-SPIONs in HUVEC cells via TEM, ICP-MS/BCA, and confocal microscopy.

Transmission Electron Microscopy: PEG-SPION-internalized HUVEC cells were collected and fixed with 2.5% formaldehyde/glutaraldehyde in 0.1M Sod Cac Buffer (pH 7.4) for 2 hours at 4° C. The cells were washed 3 times for 10 minutes each and post-fixed with 1% osmium tetroxide in PBS for 1 hour. The cells were rinsed 3 times for 10 minutes each with PBS, followed by 3 rinses with ddH_2O for 10 minutes each before proceeding with the dehydration process, which was done by increasing concentrations of ethanol (30%, 50%, 75%, 100%) for 10 minutes each. Cells were then infiltrated in increasing concentration of Poly/Bed 812 solution (Poly/Bed, DDSA, NMA, DMP-30 with weight ratio 25.5:13.5:10.9:1 respectively) in ethanol (1:3, 1:2, 1:1) for 1 hour each on a shaker, and finally 100% of Poly/Bed 812 solution overnight to allow in complete infiltration. Cells were embedded in a mold using an embedding solution (Poly/Bed 812 Embedding Media, DMP-30) to be polymerized at 60 ° C for 24 hours. Samples were cut using the Leica EM UC7 ultramicrotome. The samples were stained with 4% uranyl acetate for 4 minutes followed by 2% lead acetate for 5 minutes. Finally, TEM was conducted using Thermofisher Talos F200X at an accelerating voltage of 200kV.

Quantitative Analysis of PEG-SPIONS Cellular Uptake*:* To further quantify the amount of PEG-SPIONs internalized by the cell, the ratio of iron to the total content of protein (serum albumin) was measured using both ICP-MS and BCA, respectively. Following HUVEC treatment with PEG-SPIONs (0, 50, 75, 100, 125, 150 μg/ml), cells were rinsed with PBS gently. Then, HUVEC cells were harvested using 0.025% trypsin/EDTA and pelleted (centrifuge at 200 G) for 5 minutes at 4 °C. The supernatant was removed, and the pellet treated with 1 X RBC lysis buffer. To quantify the amount of serum albumin in the lysed samples, BCA assay was

conducted by following the standard Bicinchoninic Acid protocol. Each sample was treated with the working reagent at a volume ratio of 1:8 and incubated for 30 minutes at 37 °C protected from light. Sample absorbance was then measured via a SpectraMax iD5 microplate reader at 562 nm. The calibration curve was built using 8 points measurements of pre-calibrated serum albumin protein stock (25, 125, 250, 500, 750, 1000, 1500, 2000 μg/ml). To quantify PEG-SPIONs contents, the lysed samples at a volume ratio 2:1 were digested with 70% nitric acid at 70 °C over night. Samples were then diluted to 2% nitric acid initially in ultra-high pure water. Further dilutions were performed in HPLC water with 1.5% nitric acid (10X or 100X) as needed before proceeding with iron measurements using ICP-MS. Iron content was quantified based on 5-point calibration curve of pre-calibrated 4-iron isotopes from Inorganic Ventures (^{54}Fe, ^{56}Fe, ^{57}Fe, ^{58}Fe) standards. Samples' recoveries were confirmed using 0.5 μg/ml of ^{115}In as internal standard ($\mp$5% was allowed). The detection level of ^{57}Fe isotope was chosen for relative standard deviation due to its lower limit of detection.

3.2.2 Cell Viability. Prior to seeding 8000 cells/ well, 96-well plates were coated with fibronectin (2 μg/cm^2) for 2-3 hours. Following HUVECs treatment with PEG-SPIONs (0, 50, 75, 100, 125 μg/ml), cells were rinsed with PBS gently (several washes can result in cell detachments with a magnitude proportional to PEG-SPIONs concentration, which can give a false negative in cell count measurements). Then, cells were exposed to applied magnetic field (see section 3.3.1 for specific field parameters). Cells with no magnetic field exposure were used as control. After that, cell medium was exchanged with PrestoBlue reagent in EBM-2 at a volume ratio 1:9 and allowed 30 minutes incubation at 37° C protected from light. Finally, fluorescence was measured using a SpectraMax iD5 microplate reader at excitation and emission wavelengths of 560 and

590 nm, respectively. It is worth mentioning that leaving the 96-well plates without Al-foil cover can give false negative of cell viability. We observed that when cell viability was assessed in terms of PrestoBlue incubation time, we found an increase in cell viability in all groups as the incubation time increased when compared to the controlled group (HUVEC cells with no PEG-SPIONs internalized), see Figure 3.1A. We have attributed these results to cell detachment off well surface after PBS wash in PEG-SPION-treated group. We used light microscopy to confirm this by imaging the well surfaces (see Figure 3.1B). Coating the well surfaces with fibronectin solved this problem and provided more stable and reliable results over time.

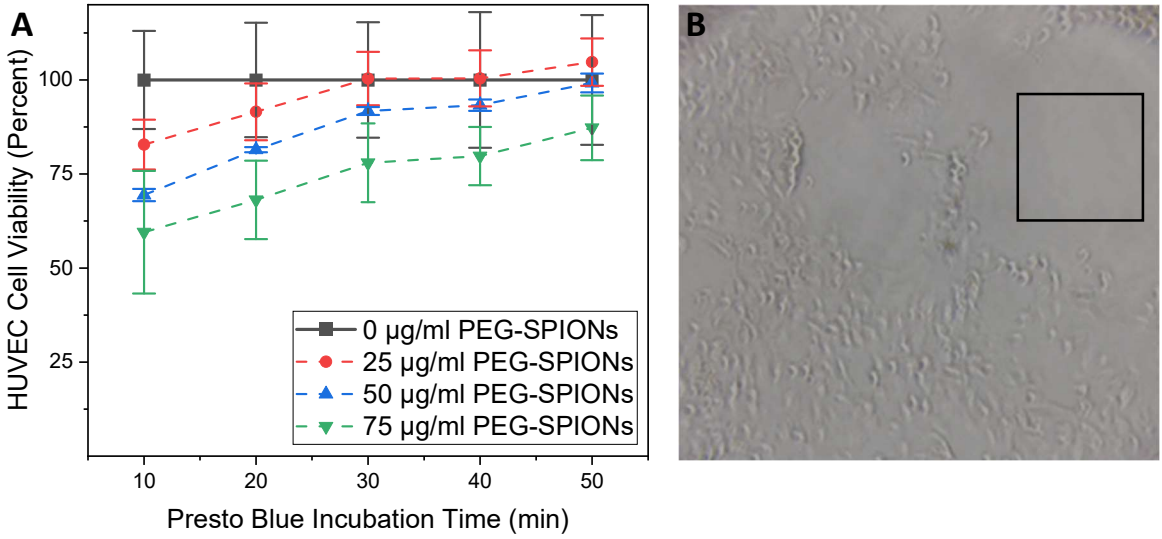

Figure 3.1 In-vitro cell viability assay limitation. (A) Cell viability studies showing inconsistent results over time when PEG-SPIONs were used. (B) Light microscope image showing HUVEC monolayers treated with PEG-SPIONs, which can cause cell detachment in uncoated 96-well plates.

3.2.3 Confocal microscopy. HUVEC cells were fixed using 2.5% formaldehyde/glutaraldehyde solution in PBS for 20 minutes at room temperature, followed by PBS wash and HUVECs permeabilization. For F-actin staining, HUVEC cells were permeabilized using 0.2% Triton-X

100 for 20 minutes at room temperature. Cells were washed three times with PBS before applying ActinGreen 488 for 25 minutes at 37° C to stain F-actin. For VE-cadherin staining, HUVECs were permeabilized using 0.01% Triton-X 100 for 5 minutes at room temperature (F-actin and VE-cadherin were not stained simultaneously). Cells were washed three times with PBS before adding 10% UltraCruz Blocking Reagent for 30 minutes at room temperature. Afterwards, cells were washed with PBS three times 5 minutes each, then 10 µg/ml of Alexa Fluor 647 conjugated to VE-cadherin F-8 antibody in PBS with 1.5% UltraCruz blocking reagent was added and incubated for 90 minutes at room temperature. DAPI was lastly added and incubated for 5 minutes at 37° C proceeding three PBS washes with 5 minutes each to remove any unbound stains. Finally, HUVEC cells were washed with PBS 3 times for 5 minutes each before applying Vectashield antifade mounting media onto the cover slips. To view PC membrane under confocal, a surgical scalpel was used to extract the membrane from the inserts to be mounted on a cover slip. For PEG-SPION staining, PEG-SPIONs were labeled with fluorophores by mixing PEG-SPIONs and 1,1'- Dioctadecyl- 3,3,3',3'-tetramethylindocarbocyanine perchlorate (DiI) in deionized water at a weight ratio of 40:1 and allowed to incubate at ambient temperature overnight. Unbound fluorophores were removed by either magnetic decantation (3 washes of deionized water) or filtering (through 0.2 µm acrodisc syringe filters with hydrophilic polyethersulfone membrane, lower yield). The size distribution of PEG-SPIONs was confirmed by DLS, and PEG-SPIONs labeling was confirmed by taking the DiI absorbance using a plate reader. Magnetic incubation of HUVECs pretreated with PEG-SPIONs has also been implemented to compensate for the low yield of PEG-SPIONs following purification process.

3.3 NanoEL 2D Model

3.3.1 External electromagnetic field Generator. During this study, a versatile electromagnetic generator (TOR 04/17 Combo, Russia) was used. The generator along with its magnetic flux mapping are shown in Figure 3.2. The unit is powered by a three-phase power line (208 V, 60 Hz), which enables alternating current (AC) generator. The unit is equipped with different sets of coils (LF, HF, Thermostat) for various combinations of field strength (up to 160 mT) and frequency (up to 270 kHz) and it is supplied with a cooling system fed by external water flow. The selection field has been characterized in terms of amplitude, frequency, and duration. The unit has been operated under the selection of LF circuit coil (maximum coil frequency is up to 271 Hz) and disabling the thermostat coils. The magnitude of the sinusoidal current was determined in terms of RMS value of 100 mT, for our measurements, with low-non heating frequency of 65 Hz, and a pulsed exposure time of 30 minutes with a 5 minute on/5 minute off pattern.

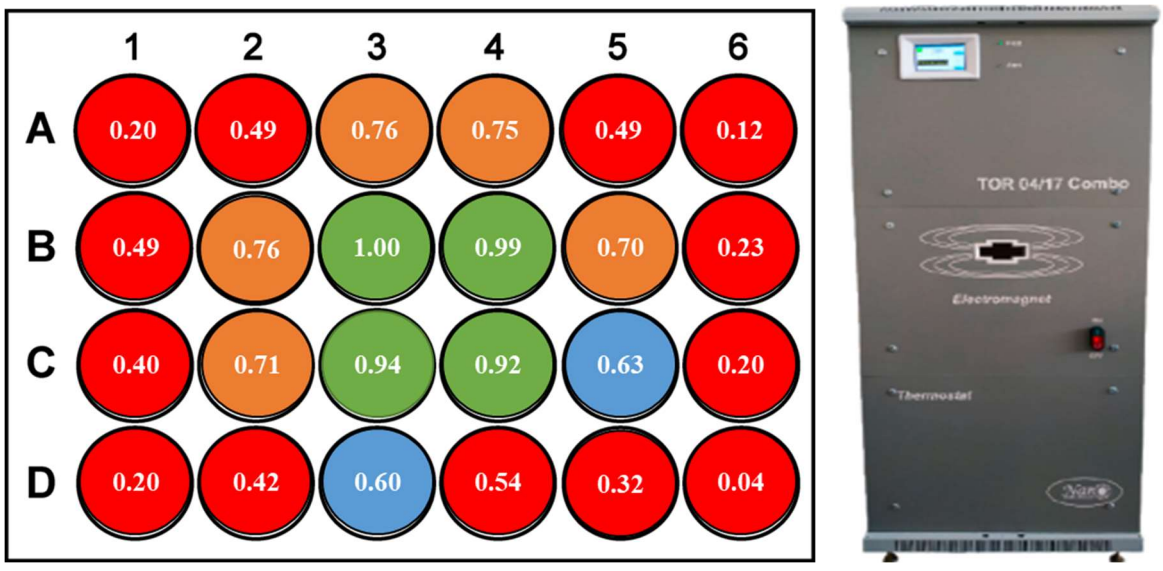

Figure 3.2 The magnetic flux mapping of the electromagnet used in this project. The mapping is specified by the vendor manual. Only the green positions were used for our experimental setup. A picture of the electromagnet is shown on the right.

Magnetic exposure was conducted at room temperature and the pulsed mode of field exposure was implemented to avoid coil overheating, and it turned out to be more effective as well. The electromagnet field generator houses a well-plate holder that keeps sample well positioned in the center of the field, which can minimize magnetic gradient variations. A magnetic flux mapping was used to determine the insert positions with relatively similar magnetic flux (see Figure 3.2).

3.3.2 In-vitro Permeability study. Polycarbonate (PC) transwell membranes (0.4 μm pore size) were first coated with fibronectin (2 μg/cm^2) for 2-3 hours and equilibrated with EBM-2 for 1-2 hours. 24-well plate transwell inserts were used with initial seeding density of 32,000 cells/insert. PC membrane is characterized by low light microscopy visibility, yet cells were maintained for 48-72 hours. Full confluent HUVEC monolayers were confirmed by either incubating 1 mg/ml FITC-dextran for 30 minutes and measuring permeability percent of FITC-dextran (5% leakiness is allowed), or by confocal microscopy (see Figure 4). Following HUVEC treatment with PEG-SPIONs (100 μg/ml), cells were rinsed with PBS gently (Longer incubation times cause particle agglomeration on cell surfaces, which cannot be washed easily with PBS. Several washes can result in cell detachments, which can give a false positive in permeability measurements). Before magnetic field exposure, FITC-dextran (700 μg/ml) in EBM-2 was exchanged with cell medium and added to the inserts as a fluorescent tracker. Finally, after the electromagnetic field exposure (see section 3.3.1 for specific field parameters), FITC-dextran was allowed to pass through the PC membrane for a minimal of 30 minutes before measuring its fluorescence using a SpectraMax iD5 microplate reader at different time intervals (FITC excitation wavelength is 490 nm and emission wavelength is 520 nm). To quantify FITC-dextran that passed through the PC membrane, only its fluorescent intensity in the wells were measured. To determine permeability

percent, the ratio of its fluorescent intensity in the wells to that remained in the inserts were measured (see Figure 3.3).

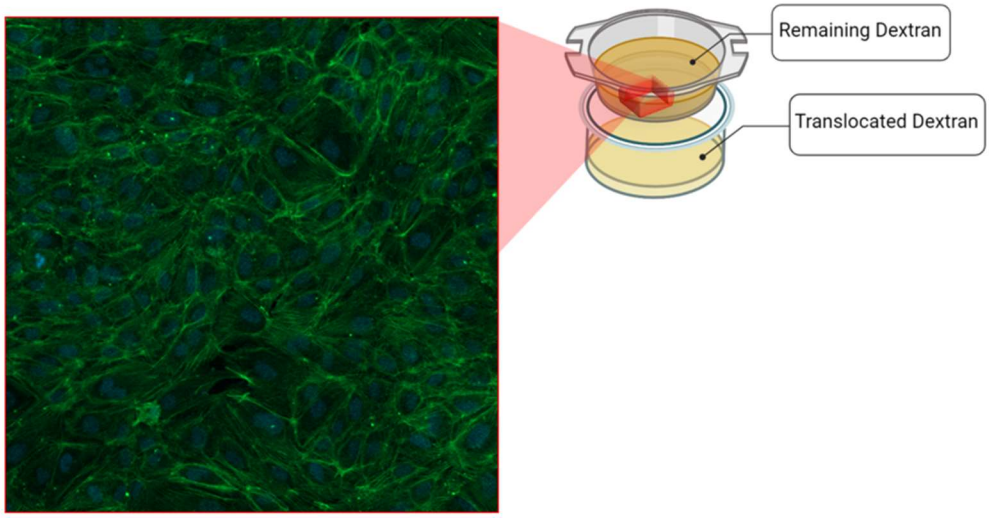

Figure 3.3 Continuous Monolayer Formation on Transwell Membrane. The monolayer is confirmed via confocal imaging. An illustration of the transwell on the left is shown.

CHAPTER 4: Results and Discussion

4.1 Physicochemical characterization of PEG-SPIONs

PEG-SPION characterization establishes a guidance to understand the behavior of these nanoparticles in biological settings and provides a road map to understand the nature and magnitude of the stress induced by MMA.

First, the core size of PEG-SPIONs was determined by TEM (Figure 4.1A). The image shows particles with relatively spherical shapes. When particles were analyzed by ImageJ, a histogram of particle size as a function of frequency is constructed (see Figure 4.1B). The histogram exhibits a normal distribution with an average particle diameter of 30 nm, which is larger than the critical size signifying that Brownian relaxation will dominate once external magnetic field is applied.

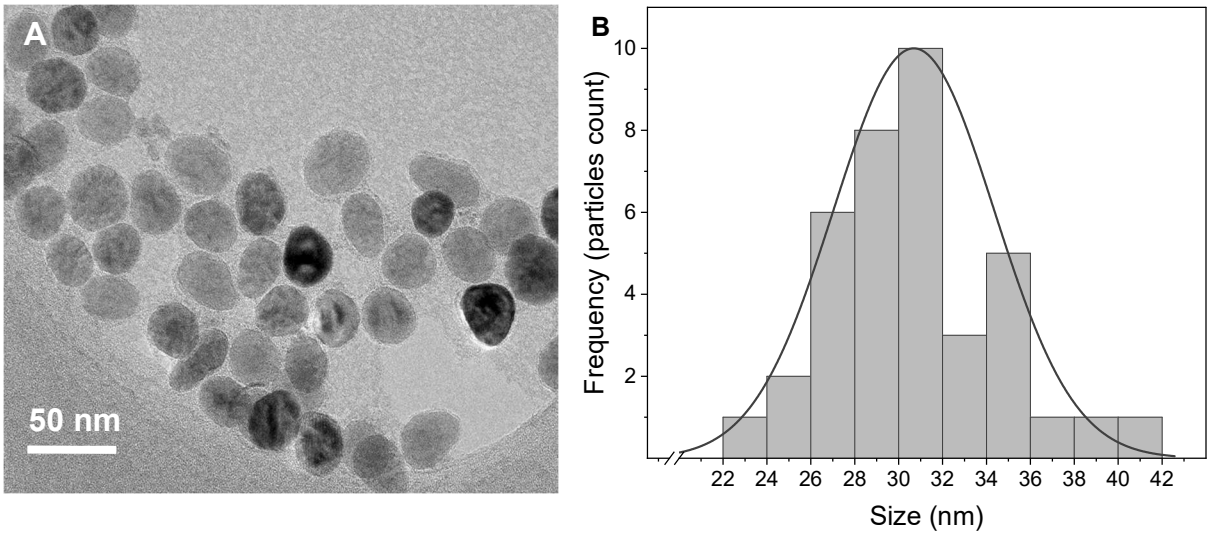

Figure 4.1 Physicochemical characterization I. (A) TEM image and (B) particle size analysis of PEG-SPIONs revealing an average particle size of 30 nm.

The elemental composition of SPIONs was confirmed via Energy-Dispersive X-ray Spectroscopy (see Figure 4.2A). The spectrum shows the characteristic EDS peaks corresponding to the electron shell transitions of both oxygen and iron. The copper peak is attributed to the TEM grid, while the carbon peak is associated with the PEG shell around the iron core. Therefore, we infer that the stoichiometric proportion of elemental iron and oxygen is consistent with that of iron oxide. The surface charge of the nanoparticles was conducted via zeta potential (Figure 4.2B) using DLS. The data indicated that negatively charged particles with an average charge of -25 mV, which explains the good colloidal stability of PEG-SPIONs.

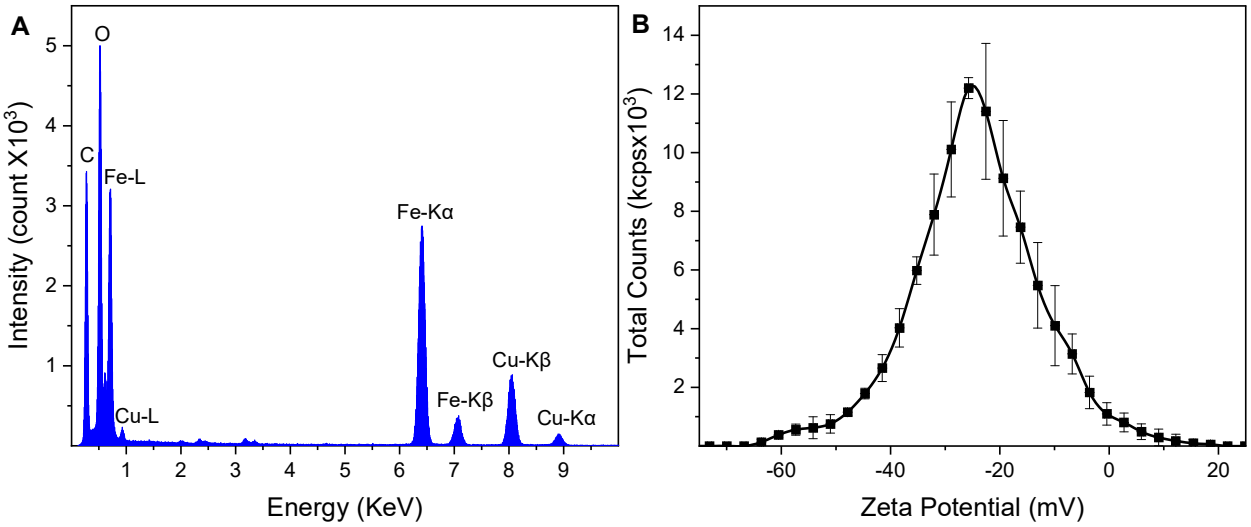

Figure 4.2 Physicochemical characterization II. (A) EDS spectrum of PEG-SPIONs showing the elemental composition of SPIONs. (B) Zeta potential profile of PEG-SPIONs.

Another requirement for colloidal stability is the successful coating of PEG on the surface of particles. From Figure 4.1A, nanoparticles are distantly apart from each other which is an indicative of PEG groups around the particle preventing their agglomeration. We have further confirmed the PEG coating using Fourier transform infrared spectroscopy (FTIR). The obtained spectrum (see Figure 4.3A) shows an asymmetric stretching at 2920 cm^{-1}, a symmetric

stretching at 2850 cm^{-1}, and a scissoring mode at 1435 cm^{-1}, which has been reported to be characteristic of hydrocarbon chain [37][38]. The peak around 1435 cm^{-1} corresponds to the CO stretching vibration mode [39]. Based on this and the presence of both CH_2 and OH peaks, we proved that the core particles are coated with PEG group.

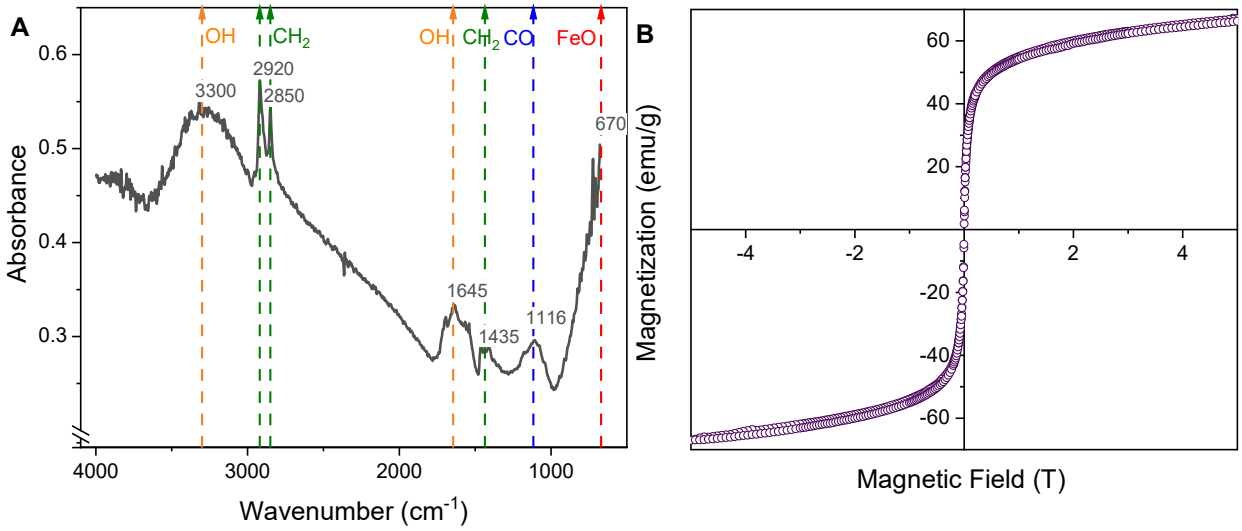

Figure 4.3 Physicochemical Characterization III. (A) FTIR spectrum of PEG-SPIONs indicating the presence of PEG layers and iron oxide cores. (B) VSM data shows the M-H curve of PEG-SPIONs measured from -5 to +5 T at 300 K. M-H curve indicates the superparamagnetic character of PEG-SPIONs.

To determine the magnetic response of PEG-SPIONs, we carried out vibrating sample magnetometry (VSM) at room temperature. The typical M-H curve of PEG-SPIONs is shown in Figure 4.3B. The curve shows nanoparticles quickly responding to applied magnetic fields with near-zero coercivity, and rapidly falls to zero when magnetic field is turned off with near-zero remanence. While PEG-SPIONs can quickly approach magnetic saturation, they do not quite reach it. This is due most likely to the non-magnetic layer (PEG). Data extrapolation suggests that the magnetic saturation is achieved at ~67 emu/g.

The last piece of PEG-SPION characterization is their stability in aqueous solution and cell culture media. The stability was examined by DLS. The initial comparison between the particle hydrodynamic size at 0 and 24 hours shows similar average size distributions (see Figure 4.4A), yet the 24 hours curve has a lower left shoulder indicating the large particles have a tendency to precipitate over time. We attribute this effect to protein corona formation due to cell medium proteins.

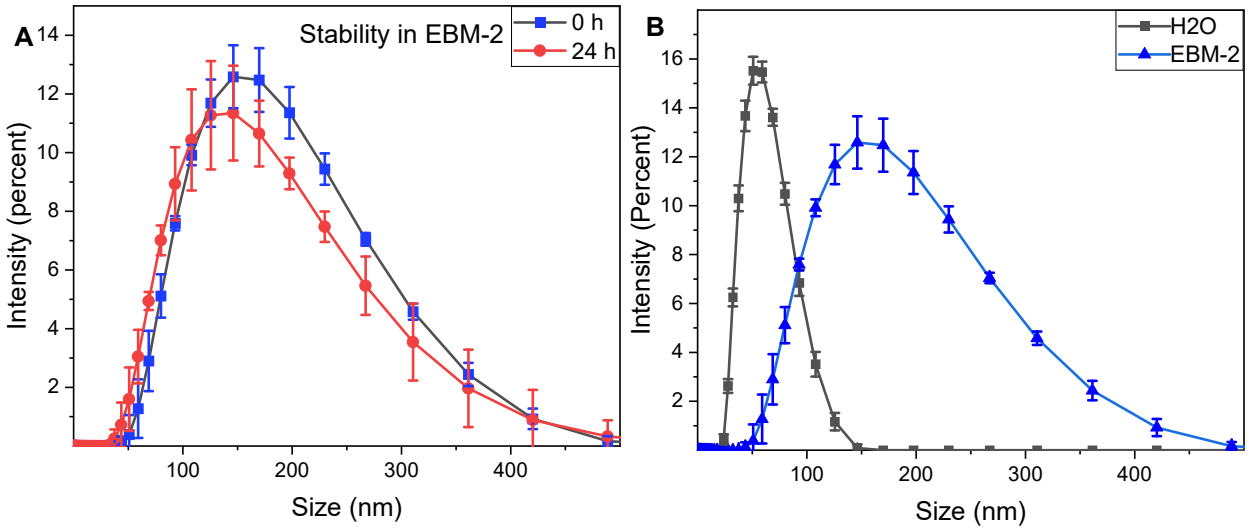

Figure 4.4 Physicochemical Characterization IV. (A) Particles' stability in cell medium described in term of hydrodynamic particles' distribution change over time. (B) Comparison between particles' hydrodynamic size in different solvents.

Protein corona formation can be thought of as a third shell of proteins encapsuling the particles and is a result of protein-PEG interaction. What supports this conclusion is the fact that the particle hydrodynamic size mean increased when particles are dispersed in cell culture media rather than water (a change from ~60 nm to ~150 nm, as shown in Figure 4.4B). The polydispersity index was found to be <0.280 for all the samples. A more detailed study on PEG-SPIONs stability in cell culture media is summarized in Table 4.1.

Solvent		Mean	STD	Min	Max
H2O at 0 h	Z average (nm)	52.54	0.01884	52.53	52.56
	Polydispersity Index (PI)	0.127	0.01424	0.1182	0.1435
	Size Disruption Mean	59.19	1.062	57.98	59.97
H2O at 24 h	Z average (nm)	58.42	0.6084	58.01	59.12
	Polydispersity Index (PI)	0.2116	0.01657	0.1949	0.228
	Size Distribution Mean	66.08	2.969	63.86	69.45
EBM-2 at 0 h	Z average (nm)	128.6	0.7481	127.8	129.2
	Polydispersity Index (PI)	0.2131	0.01981	0.1931	0.2327
	Size Distribution Mean	169.8	2.736	167.7	172.8
EBM-2 at 24 h	Z average (nm)	118.3	0.4175	117.9	118.7
	Polydispersity Index (PI)	0.2716	0.00481	0.2671	0.2767
	Size Distribution Mean	155.6	10.31	149.5	167.5

Table 4.1 Comparison of PEG-SPIONs Stability in different Solvents. DLS measurements of SPIONs in water and cell medium (EBM-2) taken at 0 and 24 hours.

It is worth noting that DLS uses Cumulants analysis algorithm to calculate the Z-average. This approach calculates the intensity weighted Z average mean size considering the polydispersity, so the reported Z average is directly measured by instrument algorithm, whereas the normal distribution is produced by data fitting. Table 4.1 shows that there is relatively more deviation between Z average and size distribution in cell medium than water at both 0 and 24 hours. This can indicate that PEG-SPIONs are more stable in water than cell medium (more instrument readings fluctuations). Further, a comparison of particles in water at 0 and 24 hours shows less increase in particle size when similar comparison is looked at in cell medium, which also suggests that particles are more stable in water than cell medium. Therefore, we have limited our

particles' incubation in cell medium to 3 hours. This limitation may only exist in vitro study because we expect that blood pressure can exert a sheer force on the particles, minimizing their interactions with other macromolecules in vivo studies.

4.2 Cell Uptake Study

In this study, the uptake of PEG-SPION by HUVEC cells is examined to see their intracellular localization and distribution. Generally speaking, a single particle exposed to an external MF would generate a force that is insufficient to induce stress on the actin filament. However, the TEM image displayed in Figure 4.5A shows PEG-SPIONs clustering in large groups across the cell. These clusters can increase the total magnetite physical radius, which is directly proportional to the induced stress force (see equation 1).

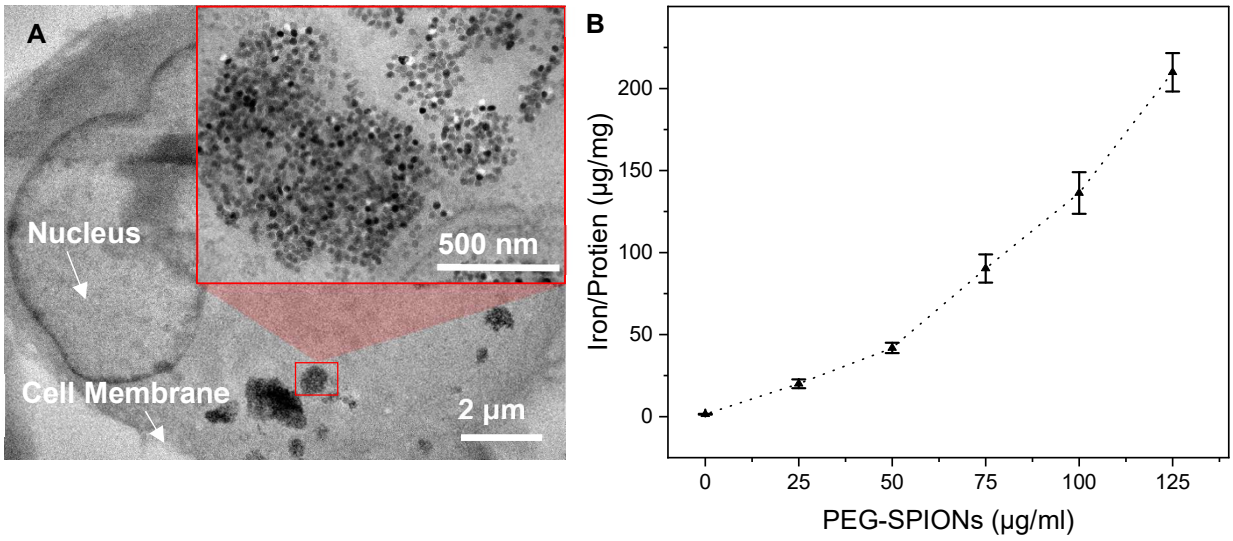

Figure 4.5. Cellular uptake of PEG-SPIONs by HUVEC cells. (A) TEM image shows the localization of PEG-SPIONs within the cells. (B) Quantitative analysis of particle uptake via ICP-MS/BCA assays. While ICP-MS measures the elemental iron contents in lysed cells, BCA measures the total content of serum albumin protein in lysed cells.

PEG-SPIONs clusters also appear to be close to the cell membrane, which is in proximity to the adherens junction.

To further quantify the amount of PEG-SPIONs internalized by the cell, the ratio of iron to the total content of protein (serum albumin) was measured using both ICP-MS and BCA, respectively (see Figure 4.5B). The results point out an increase in cell uptake as the PEG-SPION concentration increased. The cell uptake curve looks linear at low iron content; however, uptake looks more exponential at higher concentration. If cell uptake of iron is maximized, then we can further lower the number of particles used. Qiu et al showed that applying magnetic fields can significantly enhance particle uptake by HUVEC cells, as revealed by confocal and fluorescence data for cells incubated with magnetic NPs in the presence and absence (control) of external magnetic fields. Even though cell uptake can be further enhanced by magnetic incubation, the limitation of the experiment design hindered effective magnetic incubation. It is known that magnetic incubation increases the agglomeration of SPIONs and their attachment onto the PC membrane of transwell inserts. This can make particle wash (that follows particle treatment) challenging; cells become more susceptible to detachment. Additionally, if PEG-SPIONs are left on the membrane, its magnetic actuation will cause the disruption of the membrane, which can give false positive results.

4.3 Cytotoxicity Effect of PEG-SPIONs on HUVECs

To ensure safe application of PEG-SPIONs, we examined the cell viability as a function of particle concentration in the presence and absence of magnetic fields to determine the non-toxic range and toxic profile of PEG-SPIONs in HUVEC cells (see Figure 4.6). One of the goals in this assay is also to determine the optimal particle concentration that can stimulate MMA with

minimal oxidative stress activities. It is well-known that ferric ions can activate oxidative stress pathways, which can result in cell death. The cell viability assay shows no reduction in cell viability for all concentrations when PEG-SPIONs were incubated with HUVEC cells for 3 hours (Figure 4.6 A) in absence of applied magnetic fields. However, when cells treated with PEG-SPIONs were exposed to magnetic fields (Figure 4.6 B), a reduction in cell viability occurred at 125 ug/ml. Therefore, we chose 100 ug/ml as the desired concentration to conduct endothelial leakiness studies.

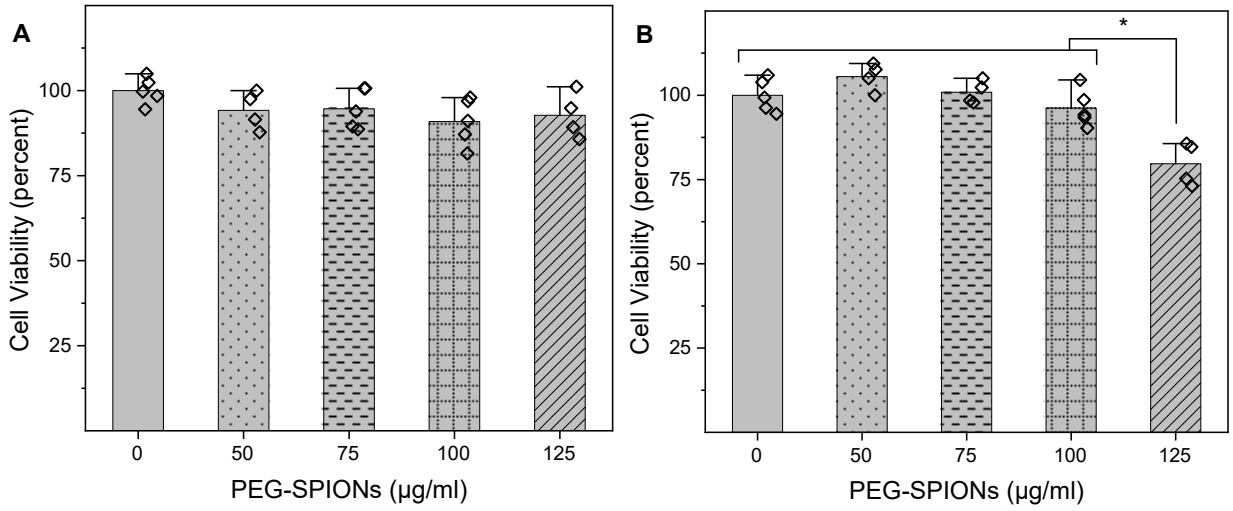

Figure 4.6. Cytotoxicity effect of PEG-SPIONs on HUVEC cells. (A) cell viability assay showing no cell viability reduction at any particle concentration in the absence of an applied magnetic field (mean+SD). (B) Cell viability assay of post magnetic field exposure (100 mT, 65 HZ, 30 min) showing no significant reduction in cell viability up to 100 µg/ml (mean+SD, * $p<0.02$).

4.4 In Vitro NanoEL by Magneto-Mechanical Actuation

To develop a non-invasive method for the induction of endothelial leakiness, we followed a magneto-mechanical strategy using a 2D cell culture model that mimics the first barrier

encountered by drugs. This simple yet powerful method represents an innovative alternative to deliver effectively therapeutic drugs across the endothelium, and can overcome issues related to the dependence on tumor heterogeneity in the complex EPR effect. A schematic illustration of our method is shown in Figure 4.7. We used transwell inserts, which contain polycarbonate-based membranes with a pore diameter (0.4 μm) small enough to prevent HUVEC cells (average size ~20 μm) from crossing the membrane. Before HUVEC cells were seeded, the membrane was coated with fibronectin, which facilitated that cells to adhere to the membrane and proliferate until forming a full continuous monolayer. Since the membrane exhibits very low cell visibility under light microscope, we used confocal microscopy to confirm the monolayer formation.

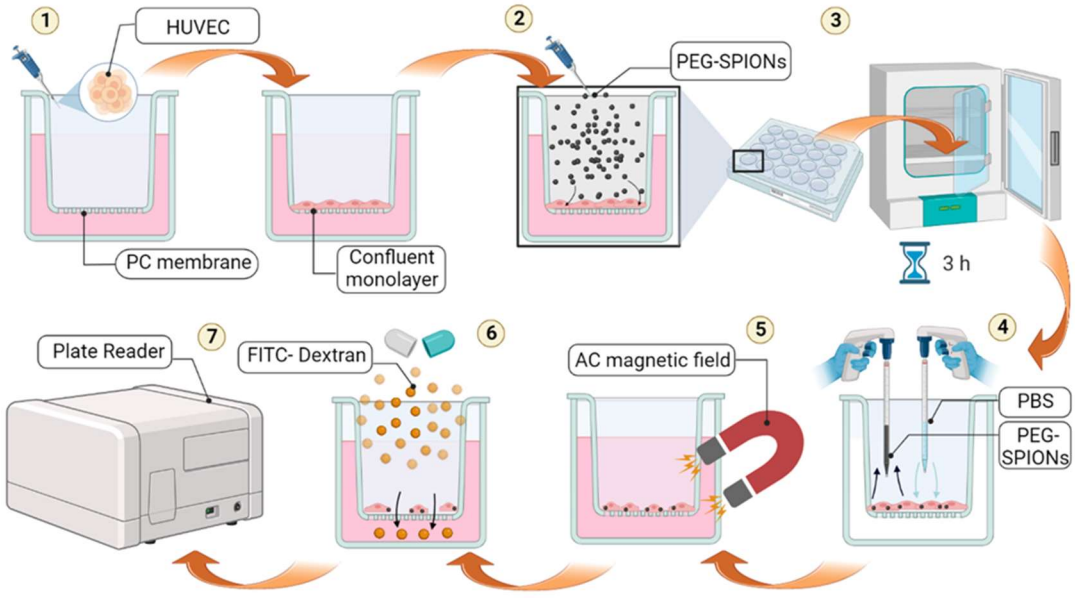

Figure 4.7 Schematic illustration of our magneto-mechanical method to induce NanoEL using a 2D cell culture model. (1) HUVEC cells are seeded on transwell inserts untill a continuous monolyer is formed. (2) PEG-SPION solution is administered to the inserts. (3) Treated HUVEC cells are incubated. (4) Transwell inserts are washed with PBS to remove remaining PEG-SPIONs. (5) HUVEC cells are exposed to non-heating AC magnetic fields. (6) When NanoEL takes place, FITC-Dextran is administered to the inserts and allowed to incubate. (7) Measurements of FITC fluorescence is taken at different timepoints to measure the percentage of dextran that crosses the monolayer.

When intracellular PEG-SPIONs are actuated by magnetic fields, gaps are induced along the HUVEC monolayer. At this point, fluorescein isothiocyanate (FITC)-labeled dextran molecules (~40,000 mol. wt.) small enough to pass through the membrane pores are administered to the inserts and allowed to incubate. The fluorescence from the FITC group was used to quantify how much dextran crosses the monolayer, which is proportional to the percentage of permeability.

4.5 Effect of PEG-SPIONs Concentration on Endothelial Permeability

In this study, we are trying to answer the question: what concentration is the most effective to induce endothelial leakiness given the physicochemical characterization and nontoxic range of PEG-SPIONs? To answer this question, we need to examine the intensity of FITC-dextran that passed through the HUVEC cell monolayer treated with different concentration of PEG-SPIONs (50, 75, 100 μg/ml). First, we looked at the 50 μg/ml of PEG-SPIONs effect (see Figure 4.8).

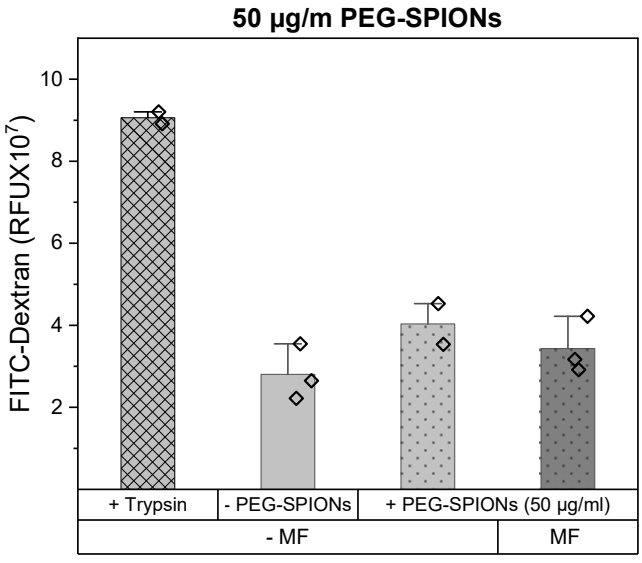

Figure 4.8 The Effect of PEG-SPIONs at 50 μg/ml on Endothelial Permeability. Quantification of FITC-dextran that passed through the HUVEC monolayer treated with PEG-SPIONs (50 μg/ml) at 1 hour of post magnetic field exposure.

The data show no statistically significant difference among the group treated with PEG-SPIONs, group treated with PEG-SPIONs and exposed to MF, and untreated/unexposed group. Since no difference is observed, we needed to use an additional control group to establish a comparison level that can validate the results. The control group uses trypsin, which can disrupt cell monolayer and cause leakiness. The use of trypsin shows significant difference in leakiness. This can validate the effectiveness of our model in mimicking the endothelial barrier, therefore, we can conclude that at 50 µg/ml MMA is not strong enough to cause leakiness.

Secondly, we looked at the effect of PEG-SPIONs at 75 µg/ml (see Figure 4.9). Our observations revealed a significant difference between the group that was treated with PEG-SPIONs/ magnetically exposed, and the control group (not treated with PEG-SPIONs and not exposed to MF).

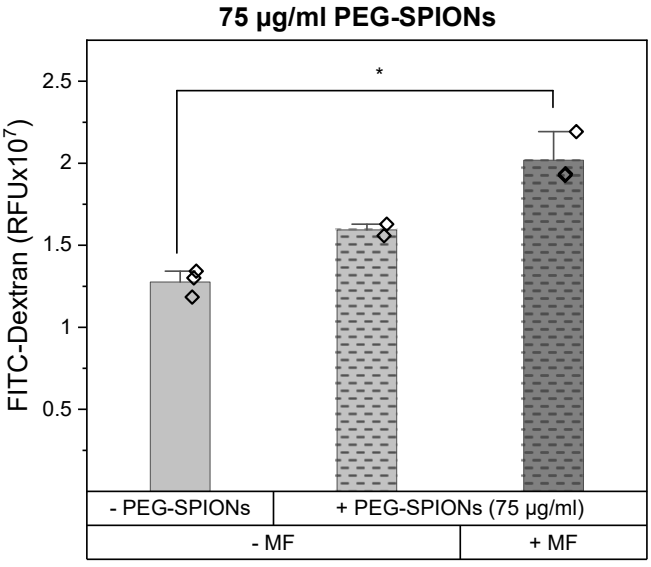

Figure 4.9 The Effect of PEG-SPIONs at 75 µg/ml on Endothelial Permeability. Quantification of FITC-dextran that passed through the HUVEC monolayer treated with PEG-SPIONs (75 µg/ml) at 1 hour of post magnetic field exposure (mean+SD, * $p<0.05$).

We also noted a direct effect of PEG-SPIONs on endothelial leakiness because the group that is treated with PEG-SPIONs, but not exposed to MF, showed relatively more leakiness than control group. This is most likely attributed to the Type-I NanoEL due to the partial participation of larger particles (detected in our DLS analysis). After quantitative analysis of FITC dextran intensity, we see that the translocated dextran has increased by 49%. Therefore, we can conclude that at 75 μg/ml MMA is effective to induce subsequent leakiness.

Lastly, we looked at the effect of PEG-SPIONs at 100 μg/ml (see Figure 4.10). That data showed a significant difference between the group that is treated with PEG-SPIONs/magnetically exposed to MF and control group. We also noted a direct effect of PEG-SPIONs on endothelial leakiness, which is attributed to the same reason discussed previously.

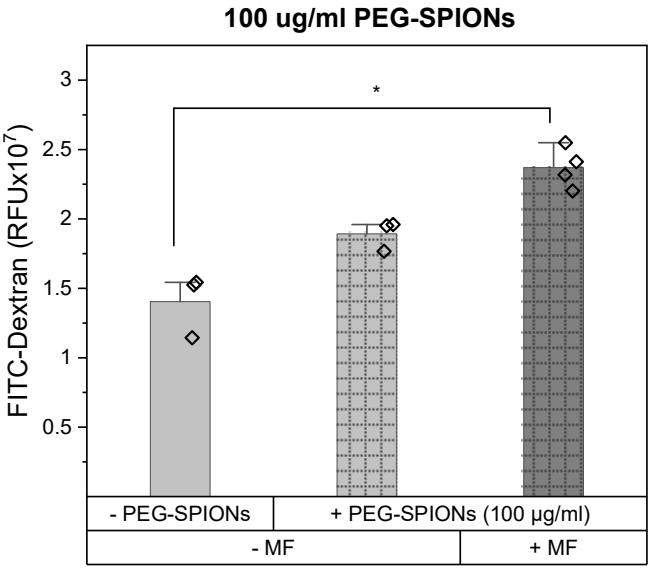

Figure 4.10 The Effect of PEG-SPIONs at 100 μg/ml on Endothelial Permeability. Quantification of FITC-dextran that passed through the HUVEC monolayer treated with PEG-SPIONs (100 μg/ml) at 1 hour of post magnetic field exposure (mean+SD, * $p<0.05$).

Leakiness quantitative analysis reveals 64 % increase in intensity of translocated dextran, which is relatively higher than the effect observed in the 75 µg/ml study (see Table 4.2). Since cell uptake is proportional with the concentration of incubated PEG-SPIONs and the induced force is proportional to particle clusters distribution, then we can infer that the endothelial leakiness is proportional to the induced force. This signifies that we can theoretically lower the concentration of PEG-SPIONs by increasing the induced force.

PEG-SPIONs	NanoEL (percent)	
	-MF	+MF
50 ug/ml	-	-
75 ug/ml	34%	49%
100 ug/ml	39%	65%

Table 4.2 Summery of percent Leakiness at different PEG-SPIONs concentrations.

To do that, we need to determine the magnitude of the induced force, which is a function of parameters we have measured. From our particle characterization data, we found that R_{HD} in cell medium is 75 nm, J_S is 35 A.m^2/kg when B is 100 mT, ρ is assumed to be ~5200 kg/m^3, and $V = (4/3)\pi R^3_{np}$ (R_{np} is 15 nm). Plugging these numbers into equation 1, we found the maximal force is ~4.8 pN acting on actin filaments anchored on PEG-SPIONs. Based on the formation of clusters, the number of particles (N) and the ordering of magnetic moments (α) within the aggregate were also considered. For the maximal force, we assume α to be 1. Based on Figure 4.5A, we can estimate the radius of the average cluster to be ~400 nm. Thus, we calculated N by taking the ratio of cluster area to that of a single particle and was found to be 498. Putting all

together, we can calculate the maximal force to be ~2.4 nN, which is sufficient to induce actin remodeling.

4.6 Effect of Post-treatment Exposure Time on Endothelial Permeability

In this study, we are trying to understand whether MMA has a prolonged effect on endothelial leakiness. Therefore, we need to look at the permeability effect over time. The results are shown in Figure 4.11 and indicate that as time progresses, the percent difference between magnetically actuated group (treated with PEG-SPIONs and magnetically exposed to MF) and unactuated group (untreated with PEG-SPIONs and exposed to MF) increased.

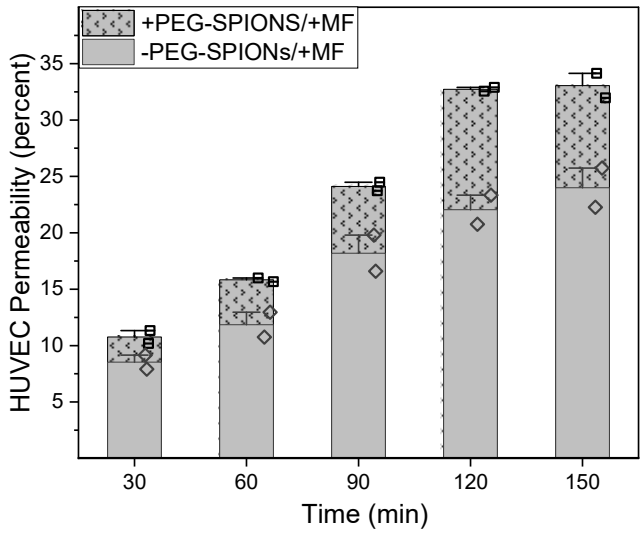

Figure 4.11 Effect of post-treatment exposure time on endothelial permeability. The relative permeability percent significantly increased with respect to time when both groups are compared.

Therefore, we can conclude that the effect of leakiness can be maximized after 2 hours post magnetic exposure. This also suggests that any clinical application can further maximize tumor

therapeutic targeting when the drug is administered after two hours. It is worth mentioning that the observed increment in leakiness for the unactuated group is a result of FITC-dextran accumulation with respect to time.

4.7 Proposed Mechanism

In this study, we propose a mechanism that can explain the endothelial permeability that is based on the physicochemical and biological changes induced by MMA at the cellular level.

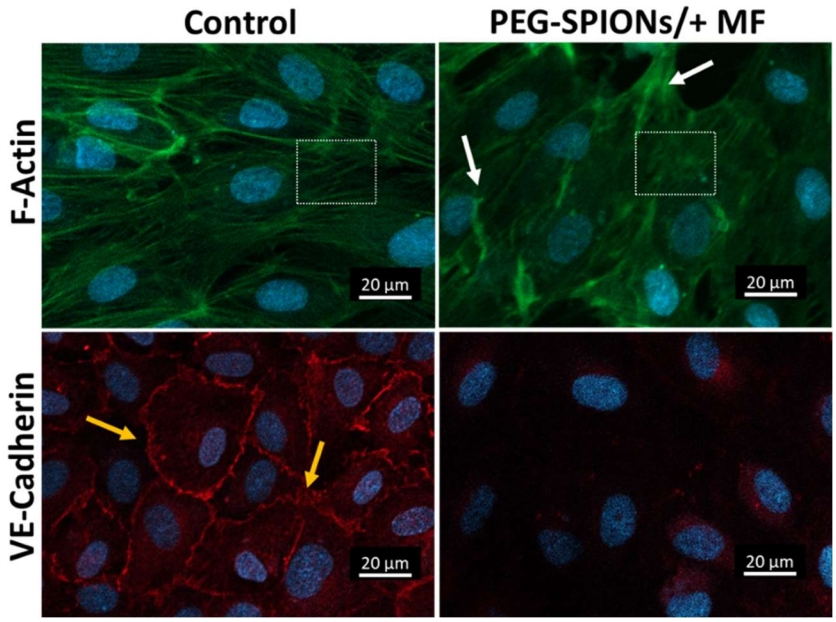

Figure 4.12 Confocal images of HUVEC cells under 20X magnification. Comparison of F-actin and VE-cadherin structures before and after MMA. White arrows show stress fiber formation, yellow arrows show intact VE-cadherins, and white dashed squares show actin remodeling.

The first point was to evaluate the subcellular components by staining primarily the F-actin and VE-cadherin and conducting confocal microscopy. Then we compare the confocal images of these components before PEG-SPION treatment and right after MMA (see Figure 4.12). The data reveal a substantial remodeling of F-actin and subsequent disruption of VE-cadherin. The

filaments of magnetically actuated cells appeared to be more elongated and well-aligned in contrast to the control group, whose filaments appear to be randomly oriented and polygonal in configuration. Additionally, the treated actin filaments seem to be denser showing more stress fibers. The disruption of VE-cadherin is observed by the absence of their confocal staining. To understand actin remodeling structure and evaluate its relationship to PEG-SPIONs, we needed to stain PEG-SPIONs and look more closely at a single cell (see Figure 4.13).

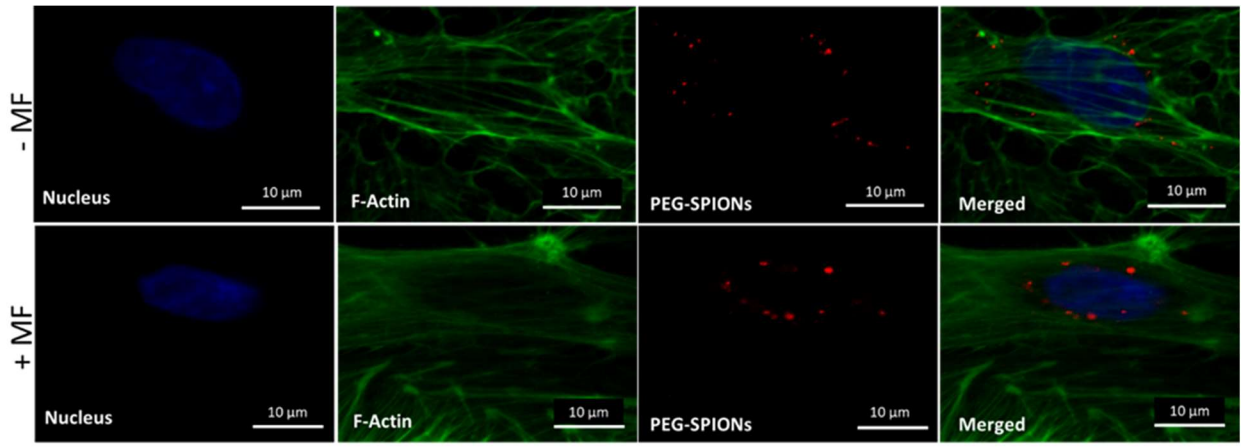

Figure 4.13 Confocal images of HUVEC cells under 65X magnification. Comparison of F-actin and VE-cadherin structures before and after MMA. Confocal images show the association of actin filaments with PEG-SPIONs and the role of the magnetic field in that association.

The particles staining show their association with the actin filaments. The images also show that when a magnetic field is introduced, particles clusters come closer to each other in comparison to non-exposed group. Further, the images suggest that the treated filaments showed a remarkable remodeling, which is characterized by filament ordering from a network-like structure into a bundle-like structure as well as the appearance of stress fibers. These results are similar to that observed in the disruption of catenin proteins and its corresponding effect on actin

polymerization by 2/3 complex (ARP2). The association of PEG-SPIONs and actin filaments also indicates that magnetic stress is directly imposed on actin filaments.

From the confocal results, we propose an educated mechanism that underlies the VE-cadherin disruption, as described in Figure 4.14.

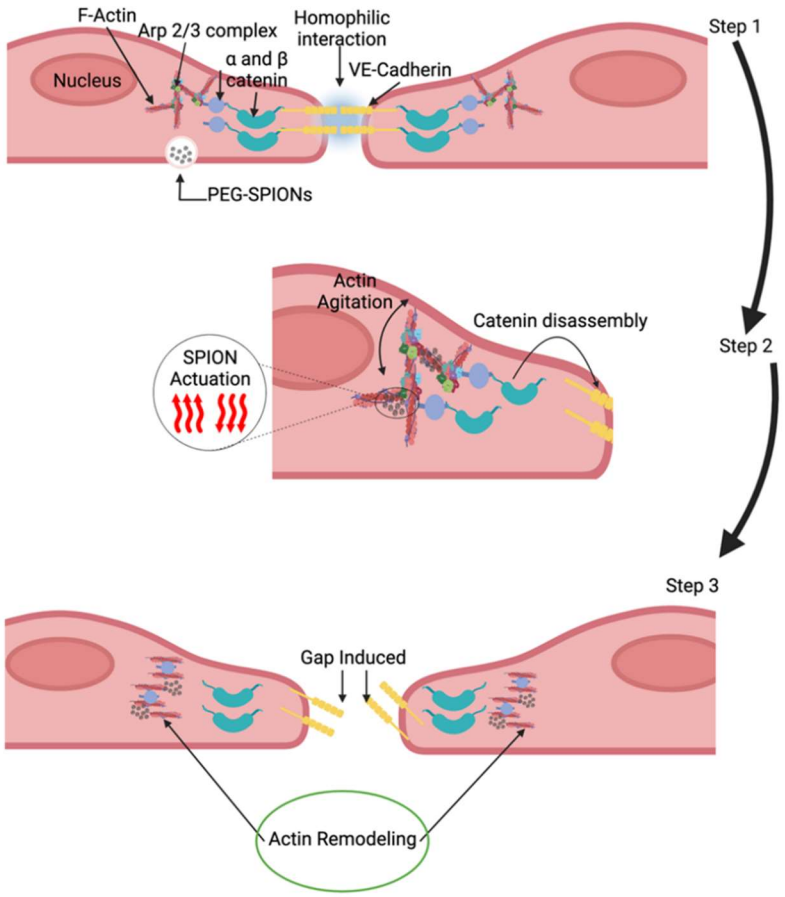

Figure 4.14 Proposed mechanism of NanoEL via magneto-mechanical actuation. Step 1 shows a full intact VE-cadherin junction before magnetic exposure. Step 2 shows the effect of MMA on actin filaments and induced cascade events that lead to VE-cadherin disruption and actin remodeling (Step 3).

Before MMA, VE-cadherin and catenin proteins are intact. However, when MF is applied, SPIONs are actuated, which in turn causes mechanical agitation over the actin filaments. The induced stress on the actin filaments leads to the disruption of the VE-cadherins homophilic interaction and catenin protein disassembly. Then, alpha catenin binds to actin proteins and competes with actin-related protein-2/3, which is responsible for actin polymerization. Alpha catenin can bring actin filament into closely packed structure, thus forcing the remodeling of the actin filaments.

CHAPTER 5: Conclusion and Future Work

5.1 Conclusion

This work has conceptually proved that magneto-mechanical actuation with the assistance of super low-frequency, alternating magnetic fields and PEG-SPIONs can enhance endothelial leakiness in a controlled manner and remotely. It also highlights the possible mechanistic pathway of VE-cadherin disruption and subsequent leakiness. While more large-scale work is needed to better understand the kinetics of this mechanism, this work establishes the basis in opening the door to implement a more controlled method to enhance tumor targeting via non-invasive MMA. Since both SPIONs and MRI have been clinically approved, then our approach is considered safe by design and has a strong potential for clinical translation. Advancing this research might be the answer to overcome today's challenges to treat cancer effectively suppressing side effects. This approach represents a non-traditional alternative to ionizing radiation and chemotherapy.

5.2 Future Work

NanoEL Recovery: While it has been reported in the literature that NanoEL can recover over time, it is therefore of paramount importance to evaluate the endothelium recovery in our approach. Such evaluation can be performed by measuring current resistance across the HUVEC monolayers. We can use an electrode to apply a voltage across the monolayer and connect it to an ohmmeter to read the cross resistance (see Figure 5.1). We expect the resistance to be inversely proportional to the number of gaps within HUVEC monolayer because the current passing through a gap encounters much lower impedance in contrast to the current passing

though the cell. Therefore, measuring the monolayer resistivity at different time intervals should provide valuable information about the monolayer recovery.

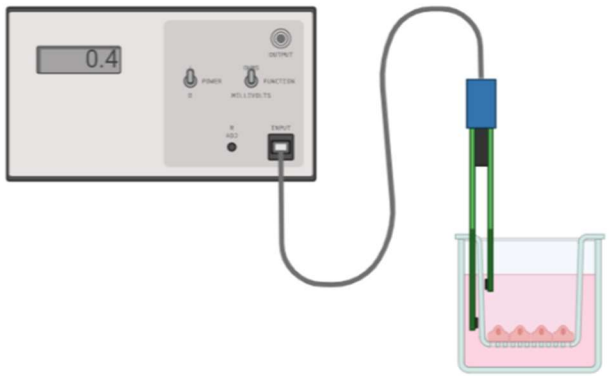

Figure 5.1. Proposed method for NanoEL recovery.

Implication of Magneto-Mechanical Actuation in Tumor Targeting: While our approach has confirmed endothelial leakiness via MMA, we still need to evaluate its effectiveness. This means that we need to see whether induced leakiness is sufficiently enough to kill cancer cells. This can also be tested in vitro using a similar model. The new model (described in Figure 5.2) should use doxorubicin (or another drug used in hospitals to treat cancer) instead of FITC-dextran, and requires seeding cancer cells (*e.g.*, T11 to treat breast cancer) on the bottom of the inserts. As MMA induces gaps in HUVECs monolayer, the therapeutic drug should pass through and kill cancer cells. Then, we can examine the cell viability using PrestoBlue Reagent. The reduction in cell viability will be sufficient enough to measure the effectiveness of MMA-induced NanoEL.

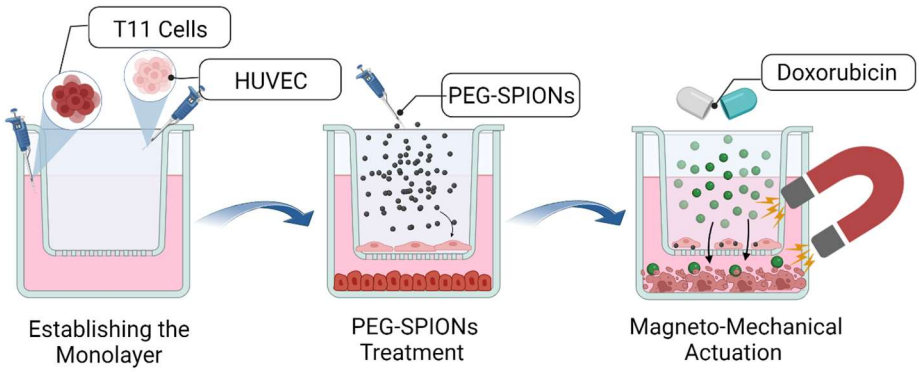

Figure 5.2. Proposed method to test drug delivery effectiveness in NanoEL via magneto mechanical actuation.

Testing the effectiveness of MMA in preventing tumor migration: We hypothesized that controlled leakiness would overcome the complication that exist in existing NanoEL approaches, such us tumor migration. To test this hypothesis, we need to check cancer cell migration and translocation from transwell membrane into the bottom of the well (see Figure 5.3). This requires choosing membranes with larger pore size (8 μm). The pore size will be selective to pass only T11 cells. Then, we can look at the bottom of the well under light microscope or even use PrestoBlue reagent to see if there is any tumor migration associated with

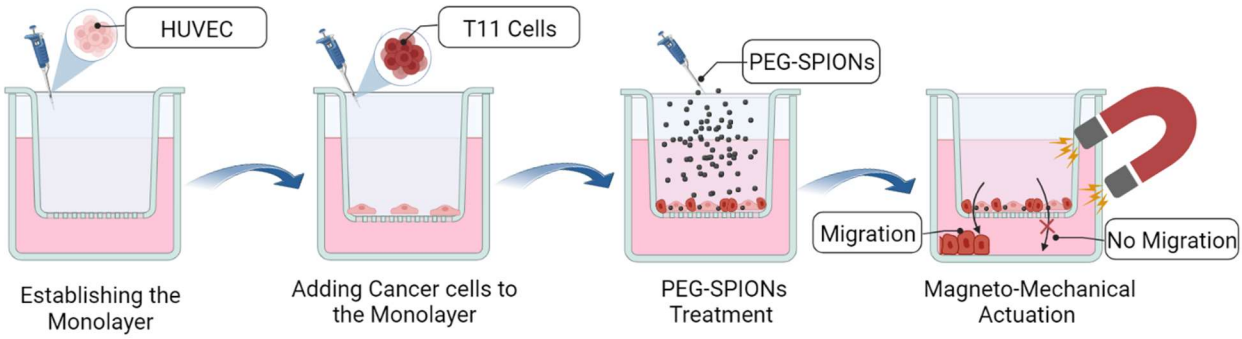

Figure 5.3. Proposed method for tumor migration prevention of NanoEL via magneto-mechanical actuation.

the leakiness. Ideally, we should not see any migration, yet due to the setup limitation, we expect to see some T11 translocation. Since some cancer cells will be directly seeded on transwell membrane pores, then we expect to see some cancer cell translocation without the need to move within the monolayer. However, when this translocation is compared to a control group, then we will be able to see if there is significant migration when leakiness is induced.

REFERENCES

[1] J. Fang, H. Nakamura, and H. Maeda, "The EPR effect: Unique features of tumor blood vessels for drug delivery, factors involved, and limitations and augmentation of the effect," *Advanced Drug Delivery Reviews*, vol. 63, no. 3, pp. 136–151, Mar. 2011, doi: 10.1016/j.addr.2010.04.009.

[2] W. Wu, Y. Pu, and J. Shi, "Nanomedicine-enabled chemotherapy-based synergetic cancer treatments," *J Nanobiotechnology*, vol. 20, no. 1, p. 4, Jan. 2022, doi: 10.1186/s12951-021-01181-z.

[3] N. Ni, W. Wang, Y. Sun, X. Sun, and D. T. Leong, "Inducible endothelial leakiness in nanotherapeutic applications," *Biomaterials*, vol. 287, p. 121640, Aug. 2022, doi: 10.1016/j.biomaterials.2022.121640.

[4] Y. Komarova and A. B. Malik, "Regulation of Endothelial Permeability via Paracellular and Transcellular Transport Pathways," *Annu. Rev. Physiol.*, vol. 72, no. 1, pp. 463–493, Mar. 2010, doi: 10.1146/annurev-physiol-021909-135833.

[5] N. Wettschureck, B. Strilic, and S. Offermanns, "Passing the Vascular Barrier: Endothelial Signaling Processes Controlling Extravasation," *Physiological Reviews*, vol. 99, no. 3, pp. 1467–1525, Jul. 2019, doi: 10.1152/physrev.00037.2018.

[6] Y. Qiu *et al.*, "Magnetic forces enable controlled drug delivery by disrupting endothelial cell-cell junctions," *Nat Commun*, vol. 8, no. 1, p. 15594, Jun. 2017, doi: 10.1038/ncomms15594.

[7] R. K. Jain and T. Stylianopoulos, "Delivering nanomedicine to solid tumors," *Nat Rev Clin Oncol*, vol. 7, no. 11, pp. 653–664, Nov. 2010, doi: 10.1038/nrclinonc.2010.139.

[8] Y. Matsumura and H. Maeda, "A new concept for macromolecular therapeutics in cancer chemotherapy: mechanism of tumoritropic accumulation of proteins and the antitumor agent smancs," *Cancer Res*, vol. 46, no. 12 Pt 1, pp. 6387–6392, Dec. 1986.

[9] J. W. Nichols and Y. H. Bae, "EPR: Evidence and fallacy," *Journal of Controlled Release*, vol. 190, pp. 451–464, Sep. 2014, doi: 10.1016/j.jconrel.2014.03.057.

[10] T. Konno *et al.*, "Selective targeting of anti-cancer drug and simultaneous image enhancement in solid tumors by arterially administered lipid contrast medium," *Cancer*, vol. 54, no. 11, pp. 2367–2374, Dec. 1984, doi: 10.1002/1097-0142(19841201)54:11<2367::aid-cncr2820541111>3.0.co;2-f.

[11] J. K. Tee *et al.*, "Nanoparticles' interactions with vasculature in diseases," *Chem. Soc. Rev.*, vol. 48, no. 21, pp. 5381–5407, 2019, doi: 10.1039/C9CS00309F.

[12] G. Bergers and L. E. Benjamin, "Tumorigenesis and the angiogenic switch," *Nat Rev Cancer*, vol. 3, no. 6, pp. 401–410, Jun. 2003, doi: 10.1038/nrc1093.

[13] A. Abu Taha and H.-J. Schnittler, "Dynamics between actin and the VE-cadherin/catenin complex: Novel aspects of the ARP2/3 complex in regulation of endothelial junctions," *Cell Adhesion & Migration*, vol. 8, no. 2, pp. 125–135, Mar. 2014, doi: 10.4161/cam.28243.

[14] F. Drees, S. Pokutta, S. Yamada, W. J. Nelson, and W. I. Weis, "α-Catenin Is a Molecular Switch that Binds E-Cadherin-β-Catenin and Regulates Actin-Filament Assembly," *Cell*, vol. 123, no. 5, pp. 903–915, Dec. 2005, doi: 10.1016/j.cell.2005.09.021.

[15] S. Yamada, S. Pokutta, F. Drees, W. I. Weis, and W. J. Nelson, "Deconstructing the Cadherin-Catenin-Actin Complex," *Cell*, vol. 123, no. 5, pp. 889–901, Dec. 2005, doi: 10.1016/j.cell.2005.09.020.

[16] A. Kobielak and E. Fuchs, "α-catenin: at the junction of intercellular adhesion and actin dynamics," *Nat Rev Mol Cell Biol*, vol. 5, no. 8, pp. 614–625, Aug. 2004, doi: 10.1038/nrm1433.
[17] D. Schulte *et al.*, "Stabilizing the VE-cadherin-catenin complex blocks leukocyte extravasation and vascular permeability: Necessity of paracellular diapedesis *in vivo*," *The EMBO Journal*, vol. 30, no. 20, pp. 4157–4170, Oct. 2011, doi: 10.1038/emboj.2011.304.
[18] M. I. Setyawati *et al.*, "Titanium dioxide nanomaterials cause endothelial cell leakiness by disrupting the homophilic interaction of VE–cadherin," *Nat Commun*, vol. 4, no. 1, p. 1673, Apr. 2013, doi: 10.1038/ncomms2655.
[19] P. L. Apopa *et al.*, "Iron oxide nanoparticles induce human microvascular endothelial cell permeability through reactive oxygen species production and microtubule remodeling," *Part Fibre Toxicol*, vol. 6, no. 1, p. 1, Dec. 2009, doi: 10.1186/1743-8977-6-1.
[20] F. Peng *et al.*, "Nanoparticles promote in vivo breast cancer cell intravasation and extravasation by inducing endothelial leakiness," *Nat. Nanotechnol.*, vol. 14, no. 3, pp. 279–286, Mar. 2019, doi: 10.1038/s41565-018-0356-z.
[21] S. Hussain *et al.*, "Carbon black and titanium dioxide nanoparticles elicit distinct apoptotic pathways in bronchial epithelial cells," *Part Fibre Toxicol*, vol. 7, no. 1, p. 10, Dec. 2010, doi: 10.1186/1743-8977-7-10.
[22] A. S. Thakor, J. V. Jokerst, P. Ghanouni, J. L. Campbell, E. Mittra, and S. S. Gambhir, "Clinically Approved Nanoparticle Imaging Agents," *J Nucl Med*, vol. 57, no. 12, pp. 1833–1837, Dec. 2016, doi: 10.2967/jnumed.116.181362.
[23] B. Thapa *et al.*, "T 1 - and T 2 -weighted Magnetic Resonance Dual Contrast by Single Core Truncated Cubic Iron Oxide Nanoparticles with Abrupt Cellular Internalization and Immune Evasion," *ACS Appl. Bio Mater.*, vol. 1, no. 1, pp. 79–89, Jul. 2018, doi: 10.1021/acsabm.8b00016.
[24] K. Murakami *et al.*, "Superparamagnetic iron oxide as a tracer for sentinel lymph node detection in uterine cancer: a pilot study," *Sci Rep*, vol. 10, no. 1, p. 7945, May 2020, doi: 10.1038/s41598-020-64926-0.
[25] Y. Huang, J. C. Hsu, H. Koo, and D. P. Cormode, "Repurposing ferumoxytol: Diagnostic and therapeutic applications of an FDA-approved nanoparticle," *Theranostics*, vol. 12, no. 2, pp. 796–816, 2022, doi: 10.7150/thno.67375.
[26] M. Nabavinia and J. Beltran-Huarac, "Recent Progress in Iron Oxide Nanoparticles as Therapeutic Magnetic Agents for Cancer Treatment and Tissue Engineering," *ACS Appl. Bio Mater.*, vol. 3, no. 12, pp. 8172–8187, Dec. 2020, doi: 10.1021/acsabm.0c00947.
[27] F. D'Agata *et al.*, "Magnetic Nanoparticles in the Central Nervous System: Targeting Principles, Applications and Safety Issues," *Molecules*, vol. 23, no. 1, p. 9, Dec. 2017, doi: 10.3390/molecules23010009.
[28] J. Estelrich, E. Escribano, J. Queralt, and M. Busquets, "Iron Oxide Nanoparticles for Magnetically-Guided and Magnetically-Responsive Drug Delivery," *IJMS*, vol. 16, no. 12, pp. 8070–8101, Apr. 2015, doi: 10.3390/ijms16048070.
[29] P. Kucheryavy *et al.*, "Superparamagnetic iron oxide nanoparticles with variable size and an iron oxidation state as prospective imaging agents," *Langmuir*, vol. 29, no. 2, pp. 710–716, Jan. 2013, doi: 10.1021/la3037007.
[30] A. Akbarzadeh, M. Samiei, and S. Davaran, "Magnetic nanoparticles: preparation, physical properties, and applications in biomedicine," *Nanoscale Res Lett*, vol. 7, no. 1, p. 144, Dec. 2012, doi: 10.1186/1556-276X-7-144.

[31] M. Sajjia, A. Baroutaji, and A. G. Olabi, “The Introduction of Cobalt Ferrite Nanoparticles as a Solution for Magnetostrictive Applications,” in *Reference Module in Materials Science and Materials Engineering*, Elsevier, 2017, p. B978012803581809264X. doi: 10.1016/B978-0-12-803581-8.09264-X.
[32] S. Wilhelm *et al.*, “Analysis of nanoparticle delivery to tumours,” *Nat Rev Mater*, vol. 1, no. 5, p. 16014, Apr. 2016, doi: 10.1038/natrevmats.2016.14.
[33] Y. I. Golovin *et al.*, “Towards nanomedicines of the future: Remote magneto-mechanical actuation of nanomedicines by alternating magnetic fields,” *Journal of Controlled Release*, vol. 219, pp. 43–60, Dec. 2015, doi: 10.1016/j.jconrel.2015.09.038.
[34] A. M. Master *et al.*, “Remote Actuation of Magnetic Nanoparticles For Cancer Cell Selective Treatment Through Cytoskeletal Disruption,” *Sci Rep*, vol. 6, no. 1, p. 33560, Sep. 2016, doi: 10.1038/srep33560.
[35] J. B. Mamani *et al.*, “In Vitro Evaluation of Hyperthermia Magnetic Technique Indicating the Best Strategy for Internalization of Magnetic Nanoparticles Applied in Glioblastoma Tumor Cells,” *Pharmaceutics*, vol. 13, no. 8, p. 1219, Aug. 2021, doi: 10.3390/pharmaceutics13081219.
[36] M. Johannsen *et al.*, “Morbidity and quality of life during thermotherapy using magnetic nanoparticles in locally recurrent prostate cancer: results of a prospective phase I trial,” *Int J Hyperthermia*, vol. 23, no. 3, pp. 315–323, May 2007, doi: 10.1080/02656730601175479.
[37] M. Bloemen, W. Brullot, T. T. Luong, N. Geukens, A. Gils, and T. Verbiest, “Improved functionalization of oleic acid-coated iron oxide nanoparticles for biomedical applications,” *J Nanopart Res*, vol. 14, no. 9, p. 1100, Sep. 2012, doi: 10.1007/s11051-012-1100-5.
[38] L. Zhang, R. He, and H.-C. Gu, “Oleic acid coating on the monodisperse magnetite nanoparticles,” *Applied Surface Science*, vol. 253, no. 5, pp. 2611–2617, Dec. 2006, doi: 10.1016/j.apsusc.2006.05.023.
[39] M. Singh, P. Ulbrich, V. Prokopec, P. Svoboda, E. Šantavá, and F. Štěpánek, “Vapour phase approach for iron oxide nanoparticle synthesis from solid precursors,” *Journal of Solid State Chemistry*, vol. 200, pp. 150–156, Apr. 2013, doi: 10.1016/j.jssc.2013.01.037.

APPENDIX: DECLARATION OF PUBLICATION

The content of this document is an expansion of a similar manuscript that is intended to be submitted to the ACS Nano journal.